

Reversible Movement of Homogeneously Nucleated Dislocations in a β -Titanium Alloy

J. P. Cui, Y. L. Hao, S. J. Li, M. L. Sui,* D. X. Li, and R. Yang

Shenyang National Laboratory for Materials Science, Institute of Metal Research, Chinese Academy of Sciences,
72 Wenhua Road, Shenyang 110016, China

(Received 2 December 2008; published 29 January 2009)

We demonstrate reversible movement of $\frac{1}{2}[1\bar{1}0](110)$ dislocation loops generated from nanodisturbances in a β -titanium alloy. High resolution transmission electron microscope observations during an *in situ* tensile test found three reversible deformation mechanisms, nanodisturbances, dislocation loops and martensitic transformation, that are triggered in turn with increasing applied stress. All three mechanisms contribute to the nonlinear elasticity of the alloy. The experiments also revealed the evolution of the dislocation loops to disclination dipoles that cause severe local lattice rotations.

DOI: 10.1103/PhysRevLett.102.045503

PACS numbers: 62.20.D-, 61.82.Bg, 68.35.Rh, 68.37.Og

Ordinary crystals start plastic deformation by the glide of dislocations generated at defects at applied stresses far below the ideal strengths of the crystals. Under special loading conditions such as nanoindentation, however, stress levels at certain locations may approach the ideal shear stress of the crystal leading to the homogenous nucleation of dislocations [1]. Alternatively, in highly anisotropic crystals where the ideal strength is much reduced, homogenous nucleation of dislocations may occur, and the barrier energy of the nucleation is reduced if it is preceded by planar lattice distortions called nanodisturbances (planar nanoscopic areas of local shear with tiny shear vectors) [2]. This mechanism was proposed to account for the plastic deformation of Gum Metals [3]. Because homogeneously generated dislocation loops are reversible in nature, they may play a role during the nonlinear elastic deformation of this type of β -titanium alloys. Experimental verification of this hypothesis is difficult, however, and electron microscope observations under an *in situ* tensile test condition must be employed.

Ti2448 alloy [4] (abbreviated from its chemical composition of Ti-24Nb-4Zr-8Sn in weight percent) is a typical β -titanium alloy that possesses peculiar elastic properties (with a very low bulk modulus that approximately equals its shear modulus of ~ 22.7 GPa) and exhibits pronounced nonlinear elastic deformation behavior. To perform the *in situ* tensile test, we chose an alloy modified from Ti2448, containing 7.6Sn. The lower Sn contents permit the reversible martensitic transformation from the β to the α'' phase [4], and it will be interesting to see how the two reversible mechanisms of homogenous dislocation loops and martensitic transformation cooperate during elastic deformation. In addition, the elastic moduli of the 7.6Sn alloy (with bulk and shear moduli of 43 and 21 GPa, respectively) differ from Ti2448 in such a way that crystal distortions are more confined to the shear planes and this should favor the nucleation of dislocations.

The 7.6Sn alloy (Ti-24Nb-4Zr-7.6Sn-0.07O) in the as-forged state consists of single β phase and exhibits non-

linear elastic stress-strain curves under uniaxial cyclic tension conducted at room temperature and a strain rate of $1.3 \times 10^{-4} \text{ s}^{-1}$ [Fig. 1(a)]. A “double yielding” is apparent, the first being regarded as corresponding to the critical stress to induce the martensitic transformation. Enlargement of the first cycle stress-strain curves up to 1% strain is shown in Fig. 1(b): clearly the nonlinear elastic deformation behavior is similar to that of Ti2448 [4].

In situ tensile tests were performed at room temperature on an FEI Tecnai F30 TEM, operating at 300 kV with a point-to-point resolution of 2.0 Å, by using a Gatan Model 654 single-tilt straining holder. The polished plate specimens were glued at the centers of Ti alloy substrates (with dimension of $9 \text{ mm} \times 2.5 \text{ mm} \times 60 \mu\text{m}$, see supplementary Fig. 1 [5]) and thinned at the central sections by double-jet electropolishing and ion milling. They were strained by applying intermittent displacement pulses manually through a trigger switch that activated a motor in the straining holder, at a crosshead speed of $1.0 \mu\text{m s}^{-1}$. *In situ* bright-field transmission electron microscopy (TEM) and instantaneous high resolution TEM (HRTEM) images were recorded by a digital video recorder during the pause periods while maintaining the tensile load.

Before tensile loading, the β phase shows normal body centered cubic (bcc) lattice structure, as evidenced by the HRTEM image taken along [111] [Fig. 2(a)]. After the

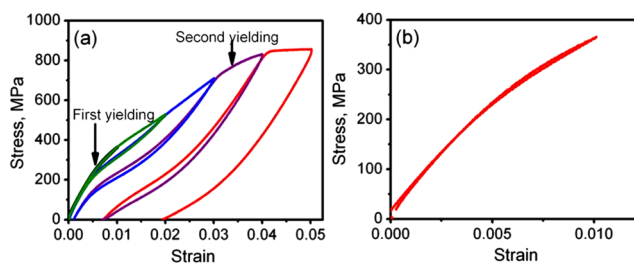


FIG. 1 (color online). Cyclic tensile stress-strain curves of Ti-24Nb-4Zr-7.6Sn-0.07O alloy with strains up to 5% at intervals of 1% (a) and enlarged version with strain up to 1% (b).

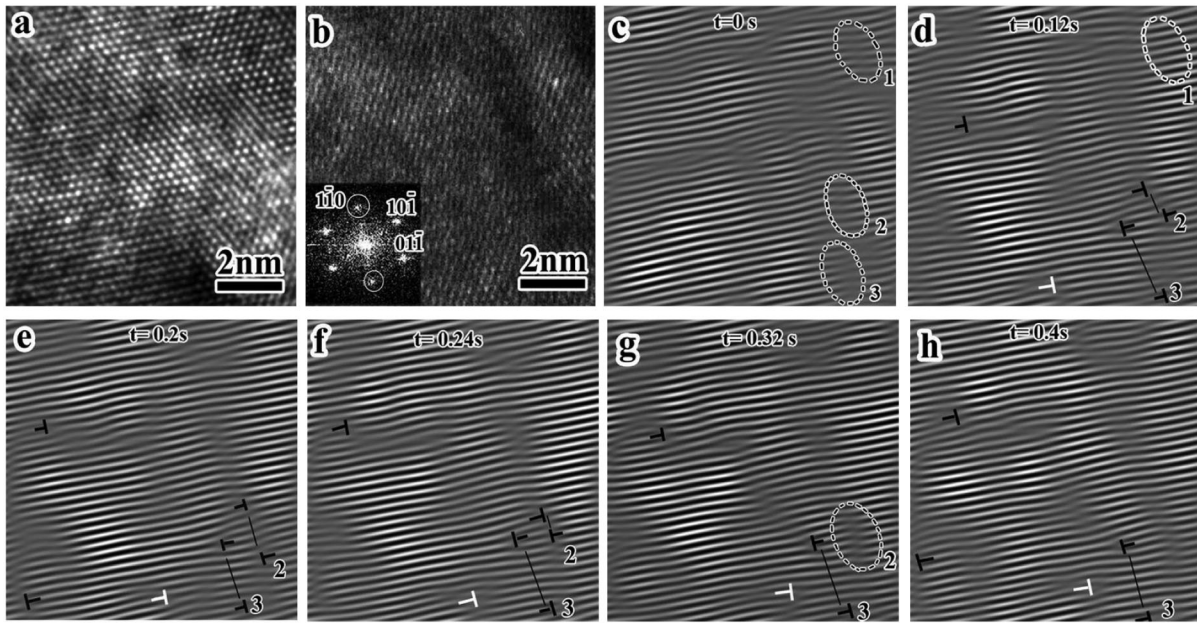


FIG. 2. *In situ* HRTEM observations to show the evolution of reversible lattice distortions and dislocation dipoles under tensile loading. (a) is a HRTEM image taken along $[111]$ before the loading and (b–h) are HRTEM frames obtained from the *in situ* recorded digital video while the load is maintained. (b) is a HRTEM image taken along $[111]$ under load at a time point set as zero (the inset shows corresponding fast-Fourier-filtered image). (c)–(h) are the IFFT images recorded at the time points noted in the figures (see text for details). The dislocation marked in white serves as a reference point.

tensile load was applied, the evolution of the HRTEM microstructure was recorded on digital video under the condition of keeping constant load (see supplementary movie 1 [6]). Although the HRTEM frames in the record were moving under straining, the structural evolution of a given region could be depicted by a series of individual still frames at different times. An initial time ($t = 0$ s) was set as the beginning of the series of HRTEM images, showing lattice distortions of a given region [Fig. 2(b)]. To present the lattice distortions clearly, inverse fast-Fourier-transformed (IFFT) HRTEM analysis was performed in this study. From three pairs of $\{110\}$ spatial frequencies as shown in the inset of Fig. 2(b), three IFFT images with one dimensional $\{110\}$ plane fringes can be obtained. Comparing with the HRTEM image [Fig. 2(b)], the IFFT image with plane fringes [Fig. 2(c)] shows much more clearly bands of lattice distortions ~ 2 nm in width and involving about 6 fringes, whereas the other two IFFT images, with $(01\bar{1})$ and $(\bar{1}01)$ plane, show nearly perfect fringes (not shown here). These distorted bands are equivalent to the nanodisturbances as defined by Gutkin *et al.* [2] To trace the evolution process of these local lattice distortions under constant load, three distorted areas within the field of view, marked by ellipse 1, 2, and 3 in Fig. 2(c), were monitored by the IFFT images with plane fringes in Figs. 2(d)–2(h).

At $t = 0.12$ s [Fig. 2(d)], the distorted area 1 recovers to the perfect lattice, revealing that the generated lattice distortions, or nanodisturbances, are reversible. Areas 2 and 3,

however, develop into dislocation dipoles of zero layer height as indicated by pairs of black \perp signs in Fig. 2(d). By Burgers circuit and crystallography analyses, the Burgers vectors of these edge dislocations in each dipole were determined to be $\frac{1}{2}[1\bar{1}0]$, and these partial edge dislocations in the dipoles glide on (110) planes. These observations demonstrate the real time evolution from nanodisturbances to dipoles of edge partials as depicted theoretically by Gutkin *et al.* [2] The three-dimensional picture is that circular regions on the (110) plane with lattice distortions evolve into dislocation loops, a cross section of which is seen here on the (111) plane, with the opposite ends of the loops represented by dipoles of $\frac{1}{2}[1\bar{1}0]$ edge partials. An observation of special interest is that the arms of the dipoles can both extend and shrink. For example, within a fraction of a second while maintaining the tensile load, the two partials of the dipole in area 2 move apart first [Fig. 2(e)] before coming close to each other [Fig. 2(f)], and finally annihilate to become an elliptic region of distorted lattice again [Fig. 2(g)]. These *in situ* observations proved unambiguously that both the nanodisturbances and the homogeneously generated dislocation loops are reversible, and both qualify as mechanisms of nonlinear elastic deformation of the modified Ti2448 alloy with bcc crystal structure.

With increasing tensile stress, the edge partials of most dipoles moved away from each other. Beyond a certain arm distance the attractive force between the two partials was overcome by the lattice friction upon unloading and the

dipoles were destroyed, signifying that the sample entered the plastic deformation range. Such evolution of the dipoles results in significant changes to the bright-field TEM images [Figs. 3(a) and 3(b)], as evidenced by the formation of numerous Moiré fringe patterns in the loaded specimen. The *in situ* digital video of TEM observation showed that the Moiré fringes sensitively vary with the tensile strains (see supplementary movie 2 [7]). These Moiré fringes are associated with different regions with average size of ~ 15 nm in width and ~ 30 nm in length. The HRTEM observations showed that the Moiré fringes are nearly perpendicular to the basic lattice fringes, as can be seen from two examples of such regions taken along [110] and [111] [Figs. 3(c) and 3(d)]. Crystal rotations of these regions relative to the parent grain are 7° to 10° as can be estimated from the Moiré fringe spacings. Extension of the partial dislocations of the dipoles during deformation should be responsible for the lattice rotation. The mechanism is schematically illustrated in Fig. 3(e) where a group of spreading dislocation dipoles (spreading loops in three dimension) effectively form disclination dipoles, similar to that in mechanically milled iron [8]. Thus local lattice rotation can be realized during tensile straining by the following three steps: the formation of the nanodisturbances, homogenous generation of loops of partial dislocations from the nanodisturbances, and the extension of these loops and their alignment on successive planes. This mechanism underlies the highly localized plastic deformation of Ti2448, and explains the nucleation of nanocrystalline grains and even the crystalline-amorphous transition of the coarse-grained alloy during compression [4].

Because martensitic transformation tends to be suppressed in thin foils [9], the α'' martensite with orthorhombic crystal structure was only found ahead of propagating cracks during the *in situ* tensile analyses. The results are consistent with a previous conclusion that the martensitic transformation is reversible between the β phase and the

α'' martensite [10], as supported by the reversible change of the selected-area diffraction (SAD) pattern during cyclic loading and unloading. The stress-induced α'' martensite, however, does not have the typical long needle or plate morphology [10]. Bright-field TEM [Fig. 4(a)] failed to detect its formation by microstructural characteristics, but the corresponding SAD pattern [Fig. 4(c)] shows clearly the contribution from both the parent phase and the α'' martensite. The dark-field TEM image obtained from $g_{\alpha''} = 110$ diffraction spot shows unambiguously the presence of the martensite [Fig. 4(b)], though it is not clear why the stress-induced α'' martensite assumes a fine equiaxed microstructure. Since the needle and plate morphologies have not been found during the *in situ* TEM observation, the possibility that needles or plates are broken by plastic deformation is excluded. It is likely that the presence of the nanodisturbances and homogenous dislocation loops has substantially modified the crystallography of the martensitic transformation. The fact that stress relieves faster in thin foils helped the rapid reverse transformation of the martensite to the β phase upon unloading, as supported by the change of the SAD pattern from Fig. 4(c) to 4(d).

It is clear from the evidence presented above that the three reversible mechanisms, local lattice distortions, homogenous generation of dislocation loops and the martensitic transformation between the β phase and the α'' martensite, all contribute to the nonlinear elastic deformation of the modified Ti2448 alloy containing lower levels of tin and oxygen (Fig. 1). Considering the evolution of the *in situ* microstructures with increasing tensile load, we conclude that these three mechanisms are triggered in turn with increasing applied stress (Figs. 2 and 4).

The difference in elastic response of bulk and thin foil samples is worth noting. The easy stress relief in thin foils as compared to bulk specimens means a higher load must be applied during *in situ* test to trigger the reversible deformations. In particular, the α'' martensite is much

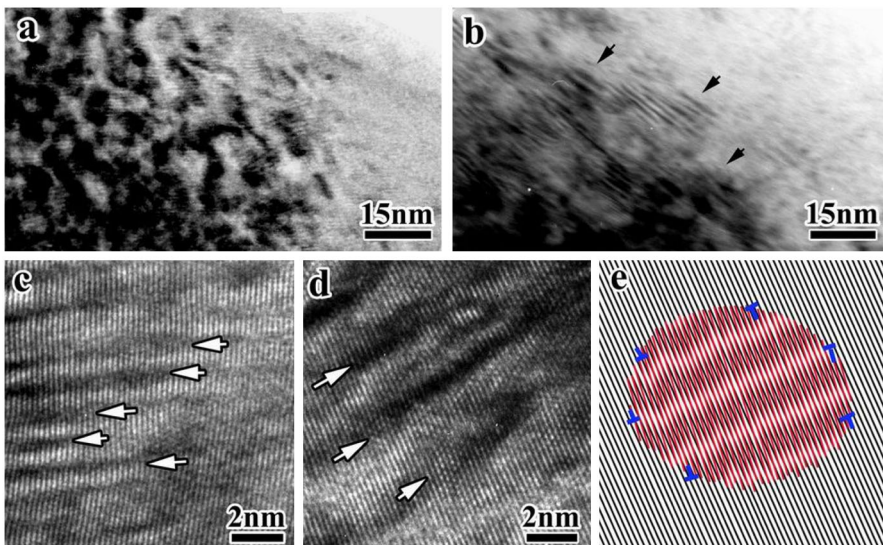


FIG. 3 (color online). Localized crystal rotations during the *in situ* tensile test. (a) and (b) are bright-field TEM images of the specimen before and after loading, respectively. The black arrows in (b) indicate the Moiré fringes. (c) and (d) are HRTEM images after loading, taken along [110] and [111], respectively; the white arrows point to the Moiré fringes which are approximately perpendicular to the basic lattice fringes. (e) is a schematic illustrating the crystal rotation of a local volume by separation of dislocation dipoles on parallel glide planes.

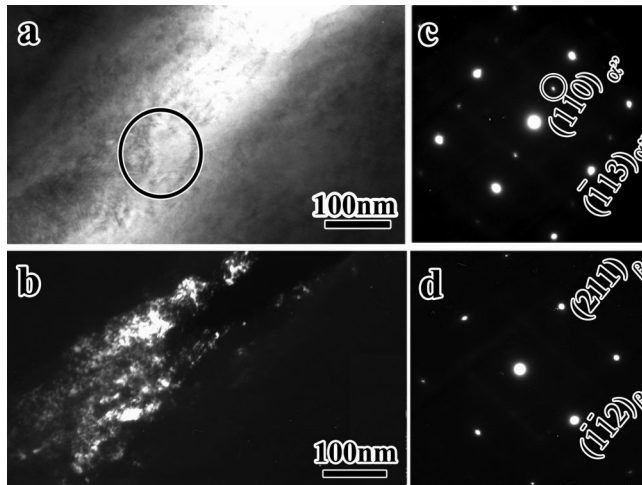


FIG. 4. The reversible martensitic transformation ahead of a crack. (a) and (b) are a pair of bright- and dark-field TEM images under the *in situ* loading, showing α'' martensite confirmed by the corresponding SAD pattern (c). After unloading, the SAD pattern changes back to that of the single β phase (d).

more difficult to form in thin foils, consistent with previous experimental results that show single β phase in thin foils but $\beta + \alpha''$ two phases in bulk specimens [4]. In spite of this difference, elastic properties of bulk samples still serve as a good basis for understanding the physical origin of the multiple reversible mechanisms observed during *in situ* tensile experiment.

The elastic instability of cubic crystals is generally triggered by the elastic softening of $C' = (C_{11} - C_{12})/2$, a modulus against tetragonal shear [10–12]. That the martensitic transformation was triggered at a stress level much higher than that causing lattice distortions and dislocation loops (Figs. 2 and 4) suggests that the bcc crystal is elastically stable at low levels of applied stress, consistent with the fact that the as-forged bulk alloy has a shear modulus of ~ 21 GPa [4]. On the other hand, its relatively low value of bulk modulus (~ 43 GPa) favors the change of lattice spacing under applied stress [4]. The combined effect of these two factors leads to local lattice distortions of the bcc crystal at the initial stage of *in situ* loading as shown in Fig. 2. Such lattice distortions would be much more significant in Ti2448 due to its much lower bulk modulus (~ 23.9 GPa) and slightly higher shear modulus (~ 22.7 GPa) [4]. The *in situ* TEM and HRTEM analyses of Ti2448 alloy are under way.

In summary, we identified reversible nanodisturbances and homogeneously generated dislocation loops before the triggering of reversible martensitic transformation as the new mechanisms of nonlinear elastic deformation of modified Ti2448, a multifunctional titanium alloy. Disclination

dipoles evolved from the dipoles of partial dislocations produce significant local lattice rotations. These rotated local volumes become the nuclei of localized nanocrystalline bands, rapidly refining the parent grains. These new reversible deformation mechanisms may guide the design of novel superelastic alloys. This work also implies that nanodisturbances as a new deformation mechanism may operate in a number of nanostructured solids deformed at high mechanical stresses, as depicted theoretically for deformed nanocrystalline materials, nanocomposites, and nanoscale solid films [13].

This work was supported by the ‘‘Hundred of Talents Project’’ of the CAS and the NSFC grants 50471074 and 50631030, as well as Chinese MOST grants 2006CB605104 and 2009CB623702.

*Corresponding author.

mlsui@imr.ac.cn

- [1] J. Li, T. Zhu, S. Yip, K. J. Van Vliet, and S. Suresh, *Mater. Sci. Eng. A* **365**, 25 (2004).
- [2] M. Gutkin, T. Ishizaki, S. Kuramoto, and I. A. Ovid'ko, *Acta Mater.* **54**, 2489 (2006).
- [3] T. Saito *et al.*, *Science* **300**, 464 (2003); S. Kuramoto *et al.*, *Mater. Sci. Eng. A* **442**, 454 (2006).
- [4] Y. L. Hao *et al.*, *Appl. Phys. Lett.* **87**, 091906 (2005); *Phys. Rev. Lett.* **98**, 216405 (2007); *Acta Biomater.* **3**, 277 (2007); S. J. Li *et al.*, *Appl. Phys. Lett.* **92**, 043128 (2008).
- [5] See EPAPS Document No. E-PRLTAO-102-020907 for supplementary Fig. 1 (Ti alloy substrates). For more information on EPAPS, see <http://www.aip.org/pubservs/epaps.html>.
- [6] See EPAPS Document No. E-PRLTAO-102-020907 for supplementary movie 1 (the evolution of the HRTEM microstructure). For more information on EPAPS, see <http://www.aip.org/pubservs/epaps.html>.
- [7] See EPAPS Document No. E-PRLTAO-102-020907 for supplementary movie 2 (Moiré fringes sensitively varying with the tensile strains). For more information on EPAPS, see <http://www.aip.org/pubservs/epaps.html>.
- [8] M. Murayama, J. M. Howe, H. Hidaka, and S. Takaki, *Science* **295**, 2433 (2002).
- [9] Y. L. Hao *et al.*, *Metall. Mater. Trans. A* **33**, 3137 (2002).
- [10] E. W. Collings, *The Physical Metallurgy of Titanium Alloys* (ASM, Metals Park, OH, 1984).
- [11] J. H. Wang, S. Yip, S. R. Phillpot, and D. Wolf, *Phys. Rev. Lett.* **71**, 4182 (1993).
- [12] C. Zener, *Phys. Rev.* **81**, 440 (1951); I. Isenberg, *Phys. Rev.* **83**, 637 (1951); E. S. Fisher and D. Dever, *Acta Metall.* **18**, 265 (1970).
- [13] M. Yu. Gutkin and I. A. Ovid'ko, *Appl. Phys. Lett.* **88**, 211901 (2006); I. A. Ovid'ko and A. G. Sheinerman, *J. Phys. Condens. Matter* **18**, L225 (2006); **19**, 056008 (2007).